HELICOPTER BLADE MORPHING STRATEGIES AIMED AT MITIGATING ENVIRONMENTAL IMPACT

ANTONIO PAGANO, SALVATORE AMEDURI
C.I.R.A, The Italian Aerospace Research Centre, Capua (CE), Italia
e-mail: a.pagano@cira.it; s.ameduri@cira.it

VALERIJAN COKONAJ
AERnnova AEROSPACE, Bilbao, Spain

ALES PRACHAŘ
VZLU, Praha, Czech Republic

ZACHARIAS ZACHARIADIS, DIMITRIS DRIKAKIS
CRANFIELD University, Cranfield, United Kingdom

The requirement of mitigating the environmental impact of helicopters has been addressed globally within the FRIENDCOPTER Project in the sense that several aspects (such as noise abatement, vibration reduction, fuel consumption) have been studied in parallel with different approaches among which there is the active blade control. In the work at hand, attention is paid on two topics aimed at mitigating helicopter environmental impact through a morphing strategy: the aerodynamic optimization of a blade section whose camber can be affected by an actuator and the design of a SMA based static twist concept, aimed at extending the helicopter flight envelope. The latter device is based on a SMA rod which is integrated in the spanwise direction within the blade structure at different positions. The actuator, when heated, transmits a torque couple which induces twist onto the blade. The twist variation due to the SMA device activation has been predicted by a FE approach (MSC/Marc software implemented with the SMA Brinson model). Finally, rotor performance in hover has been estimated with the actuator in power on and off positions, highlighting benefits coming from several spanwise integrations/distributions of the SMA device.

Key words: blade twist, airfoil camber control, SMA, morphing, main rotor

1. Introduction

Several investigations focus on main rotor performance enhancement, because of its strong influence on over-all helicopter performance (hover, forward flight, noise emission, vibration transmission at the hub, and so on). Unfortunately,

due to the variegated flight envelope characterising a helicopter mission, it is practically impossible to meet the different, often contrasting, design requirements; thus, generally, the final assessed design privileges just some flight regimes, rather penalising the others.

Among the other strategies, the possibility of adaptively modifying design parameters, thus achieving the optimal configuration for any flight condition, is at the moment object of investigation. Due to its strong influence on rotor performance both in hover and forward flight, the blade twist geometric parameter is an object of a wide amount of investigations. Envisaged benefits in terms of flight envelope extension and noise as well as and vibration attenuation, in fact, has led to quantify performance enhancement due to tailored twist distributions in Davidson *et al.* (1996), Liang *et al.* (1996) and to explore blade torsion oriented strategies (Jayasimha and Chopra, 2003). Within this scenario, the "Adaptive Material and Structure" concept, due to envisaged benefits in terms of active modification / adaptation of critical design parameters, is more and more investigated and play a fundamental role for engineering applications in the rotorcraft field (Chopra, 2002a,b).

Among the Smart Materials, Shape Memory Alloys (SMA) exhibit interesting performance in terms of transmittable forces and deformations; this, jointly with a high integration level, makes them a good candidate for static applications in different areas, from aerospace to civil field, from surgery to the electronics, and so on. In practice, the phase transformation characterising these alloys, depending both on temperature and stress field, can be exploited to recover strain (Shape Memory Effect; use as actuator element) or to endure to large deformations (Super Elastic Effect; use as non linear elastic spring (Tanaka, 1986; Buehler *et al.*, 1963)).

1D SMA components (wires, ribbons), because of related modelling and integration simplicity, are adopted for several applications; however, also substantiated by experimental approaches, more sophisticated applications are well doing for themselves. Among the others, torsional SMA technology has been also proposed in Buehler *et al.* (1963), Prahlad and Chopra (2002, 2007) for the tiltrotor where the blade twist requirements are different for hover and cruise flight.

Due to the significant influence of the main rotor on the over-all helicopter efficiency, more and more efforts focus on the maximisation of its performance for different flight regimes characterising a mission profile. Among the others, within the FRIENDCOPTER Integrated Project (2004-2009) [25], a research initiative conceived in the context of the VI Framework Programme of the European Community, dedicated strategies, aimed at enhancing the main rotor

performance in terms of figure of merit and noise emission, have been developed. The pursued idea is to suitably modify the airfoil and blade geometry in order to achieve an optimal configuration for the specific flight regime: the degrees of freedom taken into consideration, airfoil camber and blade twist angle, are controlled both statically (i.e. independently from the azimuth position of the blade) and dynamically (i.e. suddenly variable with the azimuth angle of the blade).

The former application envisages a multidisciplinary optimisation process, aimed at finding the curvature law able to assure optimal airfoil performance in terms of lift and pitching moment coefficients. A dedicated procedure, used to coordinate both commercial (meshing codes) and home made software (CFD open source code) has been defined and implemented to achieve wanted camber shape, also compatible with actuator authority: the final geometry can be achieved through small displacements, thus minimising actuator required action. As a result, different configurations, each one characterised by specific performance in terms of lift and pitching moment coefficients, have been identified.

This latter application, the static twist, described in the paper at hand, requires large angles, achievable slowly ($\approx$ 1 deg for the entire blade, at a frequency lower than 0.5 Hz). Among the different torque actuators, due to the narrow required space for integration, and to the large transmitted forces, a SMA rod has been taken into account. The peculiarity of such an actuator is that, if suitably mounted within the blade, it can transmit rotations (active element) and at the same time cooperate with the surrounding structure in absorbing external loads (structural element). The realisation of such architecture needed the synergic contribution from different disciplines. Firstly, a preliminary theoretical study aimed at predicting the blade performance has been carried out by considering the influence of the twisted cross section geometry and of the span twist distribution on the aerodynamic efficiency: as a result, the aerodynamic characteristics of the blade airfoil (i.e. lift, drag and moment coeff.) have been computed for several twist conditions and the optimal ones have been selected for the next investigations. Secondly, the problem of structurally deforming the blade to achieve required twist distribution has been dealt with; after selecting the SMA actuator typology (shape, alloy features), a FE model of the blade integrated with a SMA rod (130 mm length, with a diameter of 5.6 mm) has been realised by means of a dedicated code, MSC/Marc, implementing SMA constitutive law with Brinson's approach; required input (e.g. stress-strain curve, activation temperatures...) has been obtained through a preliminary experimental campaign. Then, a de-

dicated laboratory specimen has been designed and manufactured, both to verify the effective ability of the SMA actuator of producing torsion and to validate numerical predictions; this demonstrator is mainly constituted by an active element (a SMA rod) and a surrounding elastic structure representing the blade torque rigidity. The effective ability of inducing rotations has been demonstrated and fundamental features like time of activation vs. required power supply, performance vs. activation cycles, have been preliminary estimated. Finally, attention has been paid on the effects played by such a device on the over-all helicopter flight; by implementing the Blade Element Momentum Theory code, trim computations have been accomplished, both for the torque distribution considered during the design phase (determined by a localised SMA rod) and for other torque distributions corresponding to continuous integration of the active material along the span.

2. The rotor models

Three different rotor geometries (Enenkl, 1988) have been considered in the FRIENDCOPTER Project: the full scale rotor, its 1:2.5 model scale rotor and a novel model scale rotor with a parabolic tip (Altmikus and Bailly, 2005).

The full scale rotor and the original model scale rotor are shaped with the NACA23012 airfoil and are characterised by a rectangular planform. The new model scale rotor (see Fig. 1) mounts the ONERA OA209 airfoil on the outer part of the blade and the tip parabolic shape has been derived by the tip geometry of the ONERA/EC 7AD rotor (Schultz et al., 1996)
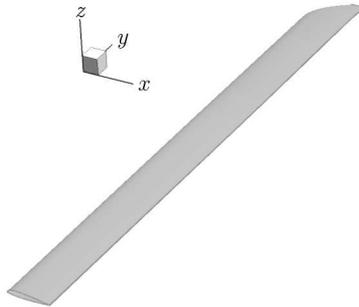

Fig. 1. View of the new model scale rotor blade with a parabolic tip

The original model scale rotor has been assumed as reference for the design of the actuators (both for airfoil camber and static twist modifications),

object of this paper; on the other hand, the new model scale rotor is supposed to exhibit passive optimization features and eventually to accommodate the installation of the actuators assessed in Sections 3 and 4.

3. First morphing concept: inner cross section dimensioning and camber optimisation

The substitution of NACA 23012 airfoil with the ONERA OA209 model in the outer part of the blade contributed to improve aerodynamic performance, as it will be shown in the following. Additional improvements can be achieved by altering through an actuator the camber of ONERA OA312. To this aim, a preliminary aerodynamic characterisation of the reference airfoil has been performed and then the optimisation task, considering given objectives and constraints, has been faced through different numerical tools. The mesh generation has been addressed by a commercial software package (Pointwise Gridgen [26]). Since the optimization is expected to require the evaluation of a large amount of different airfoils derived from the reference geometry, the computational grids have not been re-generated but an *ad-hoc* code which smoothly deforms the reference grid has been embedded within the numerical process. This fast and robust analytical mesh deformation method is based on an arc length transfinite interpolation and propagates geometric perturbations into an existing high quality initial grid while preserving the initial grid characteristics.

A C-shaped structured quadrilateral computational grid fulfilling usual requirements for turbulent calculations (refinement in the near wall region, etc.) has been generated around the ONERA OA312 airfoil. CFD computations have been carried out by means of home made software, being necessary a high access level to the source code. This CFD solver is a modified HLLC (Harten, Lax and van Leer for Contact waves) Riemann solver (Toro *et al.*, 1994) integrated within the CFD code CNS3D (Drikakis and Durst, 1994; Drikakis, 2003) to properly account for the turbulence transport quantities. WENO 5th-order schemes (Shu, 1997) have been used in the inviscid flux reconstruction discretization, while the viscous terms are discretized using second-order central schemes. The turbulence transport quantities are modelled implementing the $k - \omega$ model. Time integration is performed by a Newton method that solves the unfactored implicit equations. The implicit operator is constructed through the implementation of the flux vector splitting method of Steger and Warming (1981) along with contributions resulting from the thin layer visco-

us Jacobians and the turbulence source terms. Convergence to steady state is accelerated with a point Gauss-Seidel relaxation technique (Drikakis and Tsangaris, 1993). All these software components are a part of the computational system called MOBID (Multi-OBjective Integrated Design) assessed at Cranfield University.

The reference airfoil performance has been predicted for a range of Mach numbers and angles of attack typical of blade inboard sections by applying the Menter SST $k - \omega$ turbulence model at a Reynolds number satisfying the relation Re/Mach$\gg 8 \times 106$ and with a free stream turbulence intensity of 0.5%. The above mentioned procedure and tools have been used to predict ONERA OA312 performance in terms of lift, drag and pitching moment coefficients.

The achieved data have been compared and validated with corresponding ones obtained through an experimental campaign. Summary results (for Mach = 0.4, at 9.8 and 10.5 degrees of AoA) are illustrated in Table 1.

Table 1. Comparison between experimental and computational C_l, C_m and C_d

	AoA [deg]	C_l	C_m	C_d
Experiment	9.8	1.27	−0.0122	0.0137
	10.5	1.34	−0.0113	0.0149
Computation	9.8	1.29	−0.0125	0.0158
	10.5	1.35	−0.0115	0.0177

The optimization task is performed by using a Tabu Search (TS) algorithm that has been developed by Jaeggi *et al.* (2004). A simple and efficient geometry parameterization technique is incorporated into the numerical process. The parameterization of the initial geometry is the transformation of the active part of the airfoil into the parameterized design vector. For the employed actuator design, the active chord x_a may be varied in the range of 80% to 20%. Furthermore, it is assumed that upward and downward actuation results in the same deflection shape neglecting asymmetries from aerodynamic loading or actuator design. Furthermore, the chord length of the airfoil is assumed to remain constant. With the above assumptions, a sixth order polynomial is employed to parameterize the deformed camber line

$$f(\bar{x}) = a_6 \bar{x}^6 + a_5 \bar{x}^5 + a_4 \bar{x}^4 + a_3 \bar{x}^3 + a_2 \bar{x}^2 + a_1 \bar{x} + a_0 \qquad (3.1)$$

being $\bar{x} = [x/c - (1 - x_a)]/x_a$, c the chord of the airfoil and $x \in [(1 - x_a)c, c]$.

The authority of the actuator is introduced by the maximum achievable non-dimensional deflection $z^*_{max} = z_{max}/c$ that varies depending on the actuator design; $-0.01 \leqslant z^*_{max} \leqslant 0.01$. The polynomial function, Eq. (3.1), is

scaled by the actuator authority, thus forming the actual shape function that is superimposed to the skeleton line of the underlying airfoil

$$\Phi(\bar{x}) = z^*_{max} f(\bar{x}) \tag{3.2}$$

The design vector is constituted by 8 elements: the first 2 refer to chordwise length of the airfoil active part and the authority of the piezoelectric actuator; the remaining 6 variables represent the polynomial function coefficients and define the camber features. The optimization effort is undertaken in order to identify the aerodynamic effectiveness in terms of servo effect C_m or direct lift effect C_l of the actuation concept when applied to the ONERA OA312 airfoil. In general, the desired characteristics for an airfoil to be used in the inboard region of the main rotor blade are (1) the highest possible maximum lift coefficients at Mach numbers (Ma) from 0.3 to 0.5 for increased blade loading on the retreating side of the rotor disk, (2) pitching moment coefficients nearly equal to zero, for low blade torsion loads. From the computed polars presented in Figs. 2 and 3, it can be seen that the maximum lift, $C_l = 1.486$,
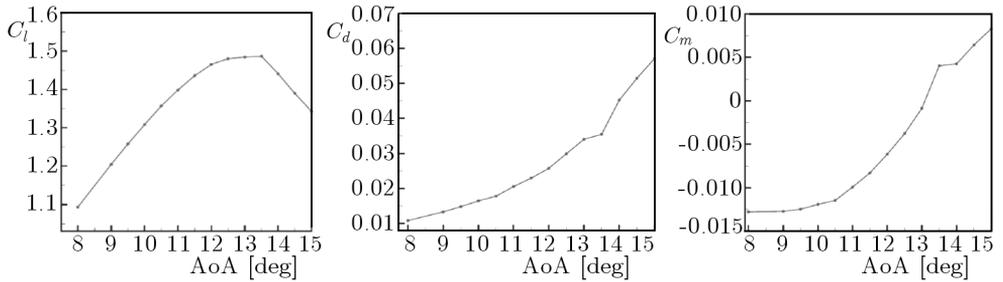

Fig. 2. Coefficients of lift (left), drag (middle) and pitching moment (right);
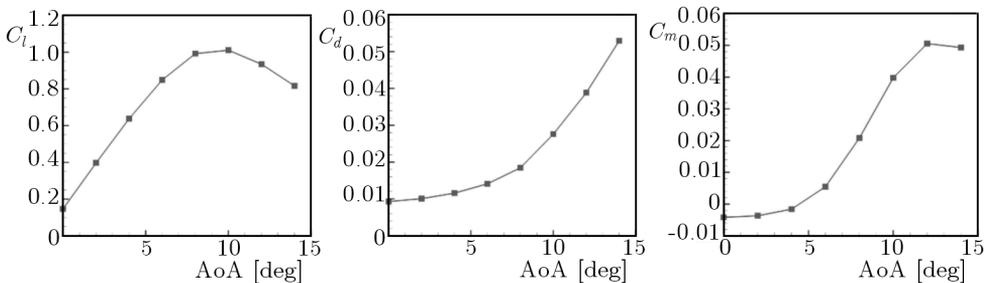Ma = 0.4

Fig. 3. Coefficients of lift (left), drag (middle) and pitching moment (right);
Ma = 0.5

occurs at 13.5 degrees for which $C_m = 0.004$ and $C_d = 0.0354$. Therefore, the design goals of the present investigation are set to be: $C_l > 1.5$ and $C_m \approx 0$.

After identifying design goals, the optimisation problem may be rewritten as the combined minimisation of the two following objectives

$$f_1 = -C_l \qquad f_2 = |C_m| \qquad (3.3)$$

also assuming as constraints the active part of the airfoil and the authority of the actuator

$$20\% \leqslant x_a \leqslant 80\% \qquad -0.01 \leqslant z^*_{max} \leqslant 0.01 \qquad (3.4)$$

Another constraint is represented by the amplitude of the polynomial itself that must not exceed unity, thus preventing from large deformations, not realizable by the actuator. This constraint is clearly satisfied by setting $a_0 = 0$ and most importantly by

$$\left| \sum_{n=1}^{6} a_n \right| \leqslant 1 \qquad (3.5)$$

After freezing the objectives and constraints, the influence in terms of computational efforts of CFD setting parameters (iterations and grid nodes) has been taken into account: in order to keep the optimization cost to a minimum without compromising in accuracy, computation grids including 280×90 control volumes are employed. The optimisation outcomes are illustrated in Fig. 4; the different discontinuities characterising the Pareto front are imputable to the non-linear nature of the aerodynamic problem.
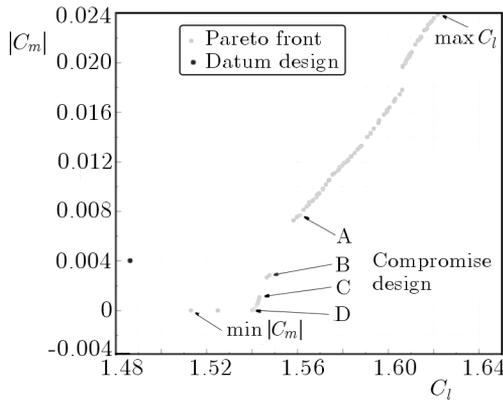

Fig. 4. Optimization Pareto front

More in detail, search pattern gaps are due to geometrically and aerodynamically unfeasible designs as well as airfoil designs of poor aerodynamic

performance. The design space appears strongly constrained in regions characterised by the lowest absolute pitching moment. In fact, the resulted feasible designs have similar values of this objective function and the trade-off surface in this area is almost horizontal, indicating that small improvements in pitching moment are obtained at the cost of lift deterioration. Furthermore, the achievable trade-off between the lift and minimum absolute pitching moment is manifested through a clear discontinuity in the Pareto front.

In Fig. 4, six designs corresponding to airfoils with, respectively, the highest lift coefficient, the lowest, in magnitude, pitching moment coefficient and some optimal compromises, are highlighted. Corresponding geometric features, quite different to the baseline and strongly differing each others, are illustrated in Figs. 5-7. The camber of the highest lift airfoil is completely different from
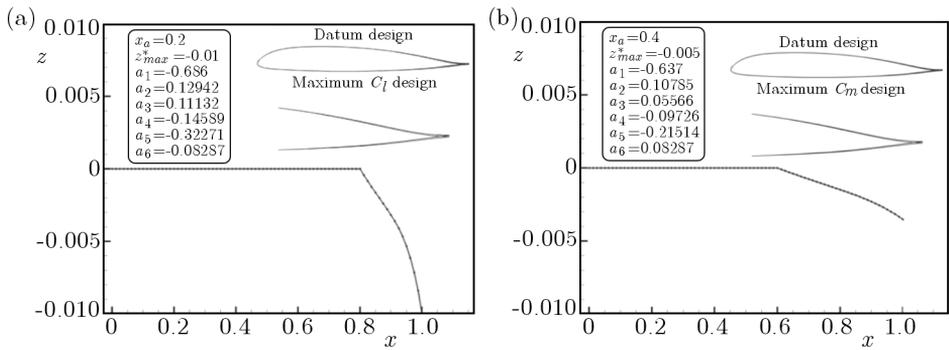

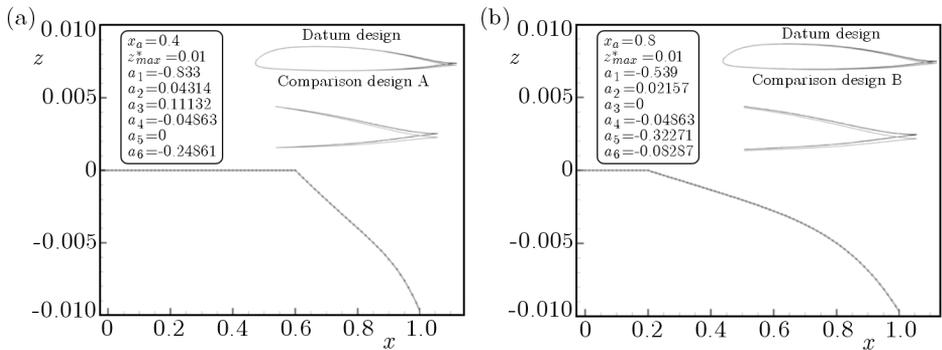Fig. 5. Maximum C_l (a) and minimum C_m (b) design

Fig. 6. Compromise design A (a) and B (b)

the lowest absolute pitching moment one. On the other hand, the compromise designs display similar geometrical characteristics with each other. Moreover,
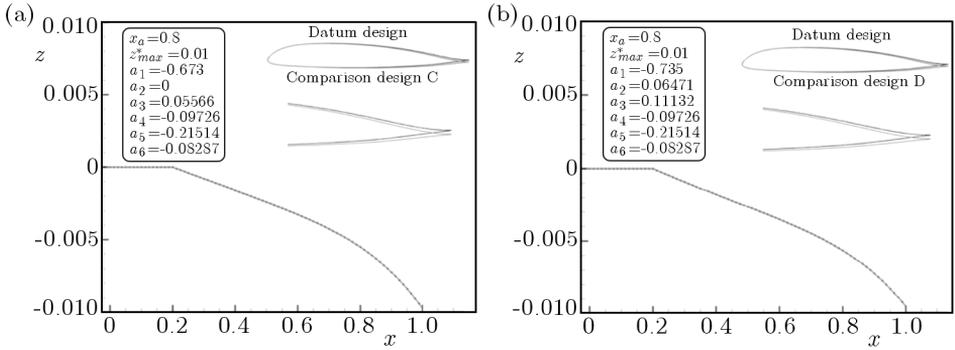
(a)

(b)

Fig. 7. Compromise design C (a) and D (b)

there are some general geometrical characteristics that distinguish the optimum designs from the baseline airfoil design. Geometries envisaging a camber increase tend to exhibit higher lift, drag and moment coefficient, because of the acceleration occurring on the suction zone. Furthermore, coherently with the optimisation process, the maximum lift coefficients are obtained with almost maximum actuator authority; in addition, design variable driving the extension of the active part of the camber achieves the lower limit of the constraint, thus magnifying the effect of the actuator authority, as it is observed from Fig. 5a. On the other hand the minimisation of the more sensitive pitching moment coefficient requires more subtle geometric changes dictating mediocre authority and active camber width as can be seen from Fig. 5b. The flow metrics of the optimization investigation are summarised in Table 2. Generally, the attainment of higher lift appears in conflict with the need for low drag coefficients and pitching moment characteristics. Nevertheless, the methodologies applied in the MOBID system result in the identification of the design vectors that reveal aerodynamic performance gains over the reference airfoil design. The Pareto front provides a clear picture of the achievable trade-offs between the competing objectives.

4. Second morphing concept: the SMA twist device

The second morphing concept considered in this work, a SMA rod integrated within the blade structure and transmitting a torque couple along the spanwise direction, is illustrated in Fig. 8. The SMA rod in charge of producing the blade torsion undergoes a preliminary twist process (pre-deformation), thus

Table 2. Comparison of aerodynamic loads amongst optimal designs

Design	C_l	C_m	C_d
Datum	1.48625	0.00403	0.03543
Max. C_l	1.62183	−0.02388	0.04079
Min. C_m	1.51211	−0.00002	0.03671
Comp. A	1.55664	−0.00763	0.03889
Comp. B	1.54586	−0.00244	0.03888
Comp. C	1.54126	−0.00063	0.03874
Comp. D	1.53842	0.00039	0.03857
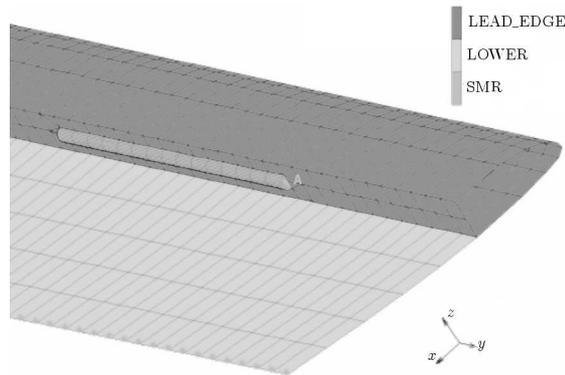
Fig. 8. SMA actuator introduced at $0.9R$ position in the rotor blade

achieving martensitic phase in no-activated condition. After integrating the rod within the blade structure, the elastic recovery of the SMA material tends to twist the blade and the consequent stress field is exploited, during the switch-off phase, for recovering the initial (non-twisted) blade condition.

A FE model has been realised by AERnnova through a SMA dedicated commercial tool, the MSC Marc/Mentat software, to predict and validate the experimental test performed by CIRA on the SMA rod specimen, whose manufacturing and testing procedure will be described in Section 6.

Preliminary considerations on main features of the SMA actuator, having as constraints the overall blade dimensions, integration requirements within the surrounding structure and actuator ability to producing the required twist (this latter aspect is described in the following Section), have allowed for identifying rod geometry parameters, that is, 5.5 mm for the diameter and 136 mm for the operative length. The assumed SMA typology, NiTiNOL 44.5%-55.5%, exhibits the properties summarised in Table 3 and measured by CIRA during a preliminary experimental characterisation of the material.

Table 3. NiTiNOL 44.5%-55.5%

	Martensite	Austenite
Young's modulus [GPa]	8.78	28.16
Poisson's modulus	0.33	0.33
Thermal expansion coefficient [1/°C]	$6.6 \cdot 10^{-6}$	$11 \cdot 10^{-6}$
Yield stress [MPa]	834.6	896.0
Slope of activation temperatures [MPa/°C]	6.0	8.0
Transformation temperatures without stress field		
Ms^0 [°C]	Mf^0 [°C]	As^0 [°C]	Af^0 [°C]
10	-20	39	82
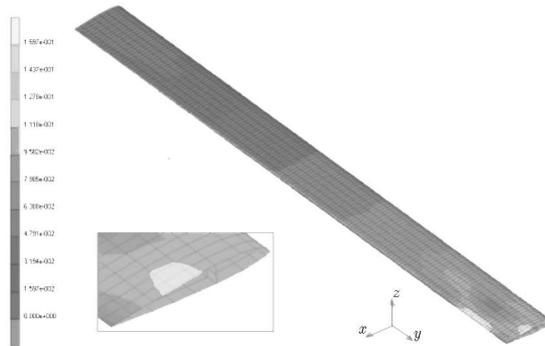
Fig. 9. Rotated angle variation spanwise with SMA actuator at $0.9R$

At first, two kinds of investigations were performed: a thermal validation aimed at demonstrating how the SMA rod changes its internal structure with temperature (Shape Memory Effect, SME) and the maximum recoverable angle validation, to make a comparison with CIRA experimental characterization. Once validated with the experimental results, the next step was the integration of the SMA rod thermal actuator at different positions along the rotor blade FE model (Figs. 8 and 9), thus comparing the obtained tip twist angles to identify the optimal location of the actuator along the span. If the priority is to achieve the highest twist angle at the blade tip, the optimum spanwise position of the SMA actuator results at $0.9R$ (Fig. 10), being R the main rotor radius. In all analysed cases for this particular blade, the spanwise induced rotations present an identical behaviour, a gradual increment from the blade root to the actuator position followed by a practically constant value until the blade tip. Consequently, depending on desirable spanwise twist variation and the twist tip value, the SMA actuator could be placed at different

positions. For any SMA actuator position, it is detected a zone in its nearness with a higher twist values due to high stress concentrations which appear due to actuator insertion in the spar.
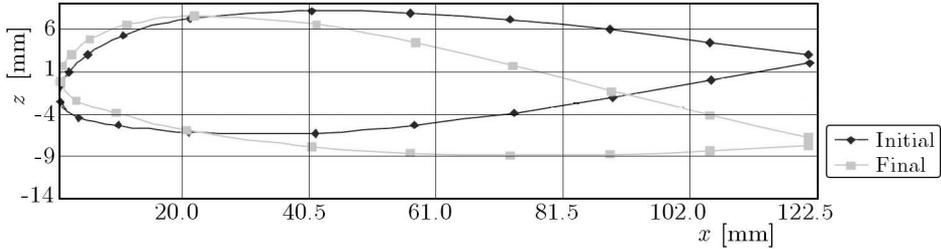

Fig. 10. Tip blade rotation with SMA actuator at $0.9R$

5. Main rotor performance

To appreciate the static twist influence on the main rotor performance, a dedicated predictive tool (Pagano, 2003) able to trim the rotor has been used. This software is based on BEMT (Blade Element Momentum Theory) which is a methodology commonly used in the preliminary design. The airfoil aerodynamics is taken into account either by assigning the properties such as the lift curve slope $C_{l\alpha}$ or the profile drag C_{do} or by extracting the aerodynamic coefficients from look-up tables. Several corrections have been implemented in order to take into account the effects associated with the Reynolds number, stall, tip losses, tip vortex.
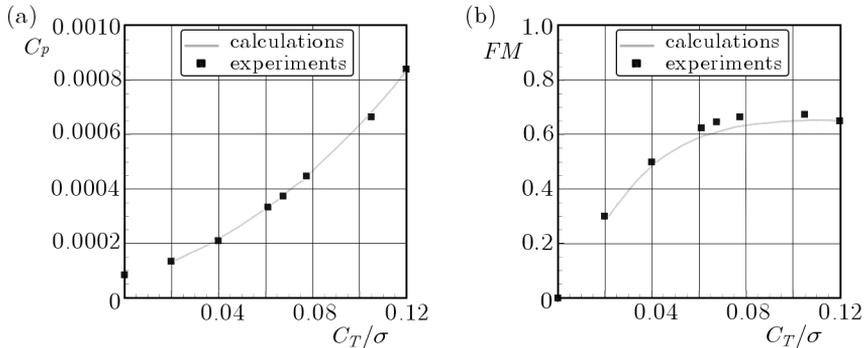

Fig. 11. Rotor performances of the full scale rotor in terms of power (left) and figure of merit (right); solid line – calculations, symbols – experiments

A validation of the tool has been performed by comparing the achieved predictions on a full scale rotor data with corresponding ones, published in Warmbrodt and Peterson (1984), see Fig. 11. After this preliminary validation, the performance of the model scale rotors have been estimated and compared, as shown in Fig. 12. The effects of the parabolic tip and the influence of more aerodynamic efficient airfoils can be clearly appreciated, both in terms of figure of merit and power.
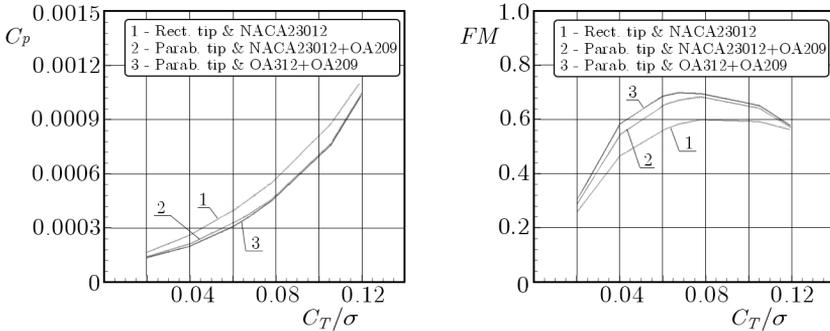

Fig. 12. Performance predictions of three model rotors considered in FRIENDCOPTER

Before dealing with the problem of actuated twist, an optimum angle distribution starting from the built-in blade twist assuring aerodynamic performance enhancement has been searched for. Later it will be controlled the possibility of reaching such distribution by means of the SMA actuator.

Five design variables have been considered to define the final optimal twist distribution. As the objective function, the weighted sum of the figure of merit at several rotor loads

$$
\left.\frac{C_T}{\sigma}\right|_1 = 0.02 \qquad \left.\frac{C_T}{\sigma}\right|_2 = 0.04 \qquad \left.\frac{C_T}{\sigma}\right|_3 = 0.06
$$
$$
\left.\frac{C_T}{\sigma}\right|_4 = 0.08 \qquad \left.\frac{C_T}{\sigma}\right|_5 = 0.10 \qquad \left.\frac{C_T}{\sigma}\right|_6 = 0.12
$$

(5.1)

with the constraint of a maximum sectional twist increment lower than 1 degree, has been assumed

$$
\left.FM\right|_W = 0.10 FM\big|_1 + 0.15 FM\big|_2 + 0.25 FM\big|_3 + 0.25 FM\big|_4
$$
$$
+ 0.15 FM\big|_5 + 0.10 FM\big|_6
$$

(5.2)

As far as the design variables, they are three twist values (at the blade root, at the tip and at an intermediate user defined blade radial station), the in-

termediate radial station and, finally, a parameter that can select one of the nine twist implemented distributions (linear, quadratic, ...). The OPTIMUS [15] software has been used for performing the mentioned optimization task. This tool allows for integrating arbitrary numerical analysis codes, automating the process execution, controlling data exchanges, splitting the process over a heterogeneous computational environment analyses and post-processing results. The key functionalities of optimization methods are available for addressing the search for global optima. DOE, RSM, Gradient/Genetic based algorithms can be, respectively, used for the exploration of the design space, the approximation of models, the design optimization.

Figure 13 depicts the flowchart, oriented along left-right direction, followed by OPTIMUS software during the specific optimization task: the objectives (in black) are evaluated starting from the design variables (in dark gray) throughout the data exchange (in gray) and the analysis blocks (in light gray). Six parallel streams, one for each considered rotor load condition, are set up to account for the effect of change in twist distribution on the rotor performance.
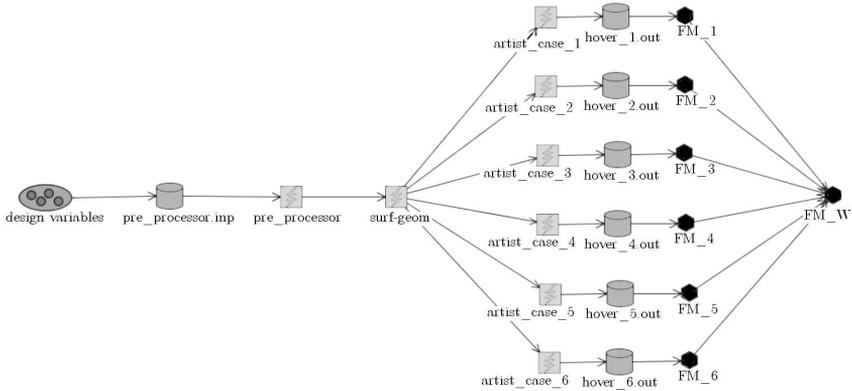

Fig. 13. OPTIMUS workflow

The pre-processor updates the input file of the surface grid generator according to the design variables set by the optimizer; after the surface grid is generated, the BEMT code computes the figure of merit for each rotor load conditions which are subsequently used to evaluate the objective function. Several optimization problems have been performed. All of them have been based on a three-level full factorial Design of Experiment (DOE) followed by a Response Surface Method (RSM) from which a differential evolution algorithm has been employed. The first problem concerns the search for an optimum twist distribution assuming that the built-in twist can be modified all over the blade or on a limited portion of it. The first assumption corresponds to

an actuator acting all along the blade whereas the latter assumption implies integration of the actuator into a given blade segment. Three cases corresponding to different blade segments where the twist variation is made possible are considered: $r/R = [0.7, 1.0]$, $r/R = [0.45, 0.75]$, $r/R = [0.275, 0.525]$. The optimum twist distributions found are represented in Fig. 14. It can be seen that nearly the maximum bound of the design space has been chosen by the optimizer (that is 1 degree) for each case. This fact suggests that actuators allowing larger twist variations are preferable. The results in terms of the objective function are collected in Table 4 from which it can be concluded that it is convenient to act on the whole blade and, as alternative, to integrate the actuator in the outer part of the blade. After these preliminary investigations, the AERnnova-CIRA concept presented in Section 4 is analysed. In this case, the actuation technology is known, that is, depending on the location where the actuator is integrated, the maximum twist variations are known. Thus, the problem consists in searching for the best place where the actuator has to be integrated and for the amount of the twist variation (provided by the actuator among the allowable ones) so that the hover performance is improved.

Table 4. Summary of results

ID	Spanwise range where twist variations are possible	Maximum allowed twist variation	$FM\big|_W$
Twist$_{ref}$	$-$	$-$	0.60947
Twist$_{all}$	$r/R = [0.22, 1.0]$	$\pm 1\,\mathrm{deg}$	0.62691
Twist$_{out}$	$r/R = [0.7, 1.0]$	$\pm 1\,\mathrm{deg}$	0.61791
Twist$_{med}$	$r/R = [0.45, 0.75]$	$\pm 1\,\mathrm{deg}$	0.61342
Twist$_{inn}$	$r/R = [0.275, 0.525]$	$\pm 1\,\mathrm{deg}$	0.61346

The actuator consists of a SMA element 135 mm long, corresponding to 6.8% of the entire blade span. AERnnova performed some numerical calculations to predict the maximum twist variation for a given number of actuator installation positions on the reference model rotor.

Since the actual twist laws all along the blade with the actuation 'on' are not available, specific twist laws are considered: in Figs. 15a, 16a and 17a, the assumed twist distributions for the SMA actuator located in the ranges [0.9-0.968], [0.7-0.768] and [0.5-0.568]r/R, for both linear (mode 1) and parabolic (modes 2 and 3), positive (green) and negative (blue) torsion are illustrated. A DOE (based on a latin-hypercube algorithm with 200 designs) is calculated using the same objective function previously defined for each actu-
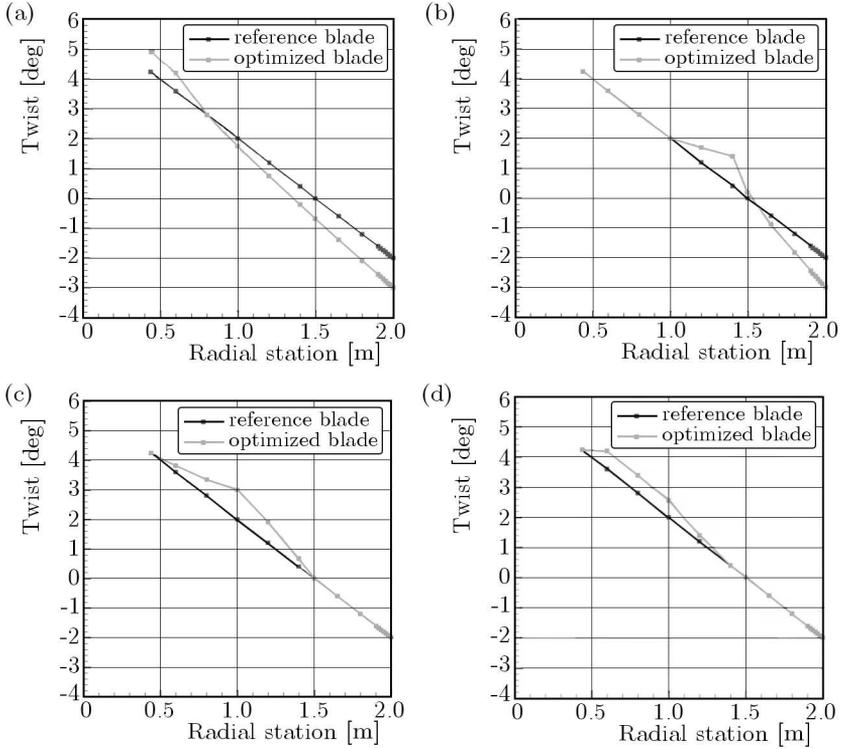
Fig. 14. Twist distribution in the case of twist variation in the range
(a) $r/R = [0.275, 1.0]$, (b) $r/R = [0.7, 1.0]$, (c) $r/R = [0.45, 0.75]$,
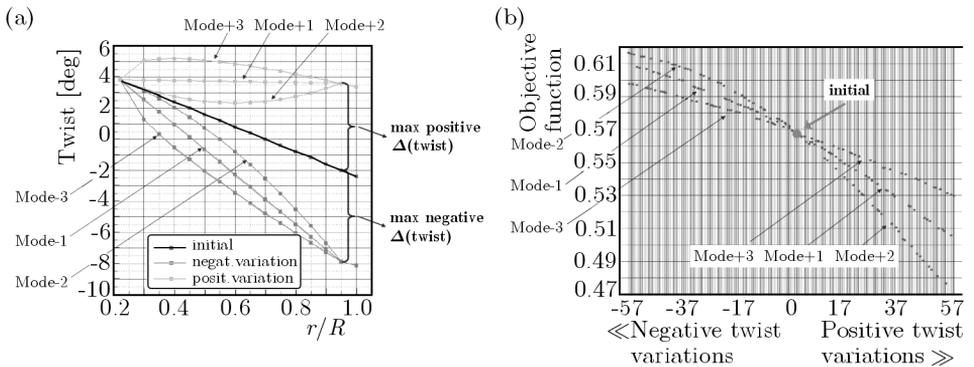(d) $r/R = [0.275, 0.525]$

Fig. 15. (a) Twist distributions: positive (light grey) and negative (grey), linear
(mode 1) and parabolic (modes 2 and 3), (b) objective function; SMA actuator
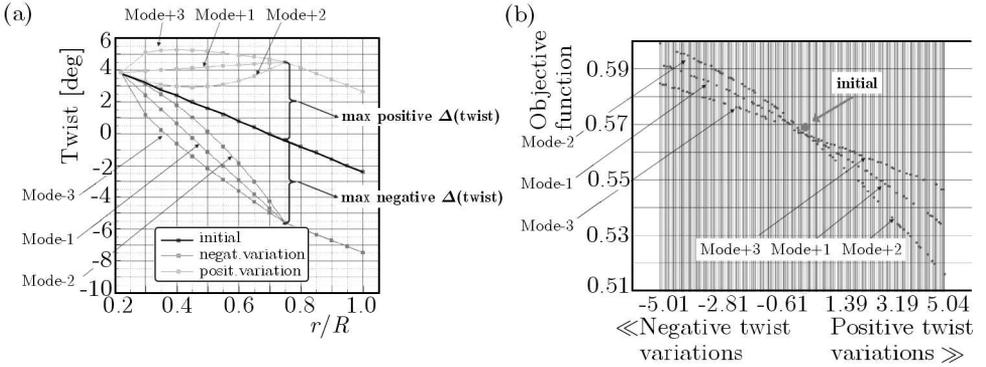located between 0.9 and $0.968 r/R$

Fig. 16. (a) Twist distributions: positive (light grey) and negative (grey), linear (mode 1) and parabolic (modes 2 and 3), (b) objective function; SMA actuator located between 0.7 and $0.768 r/R$
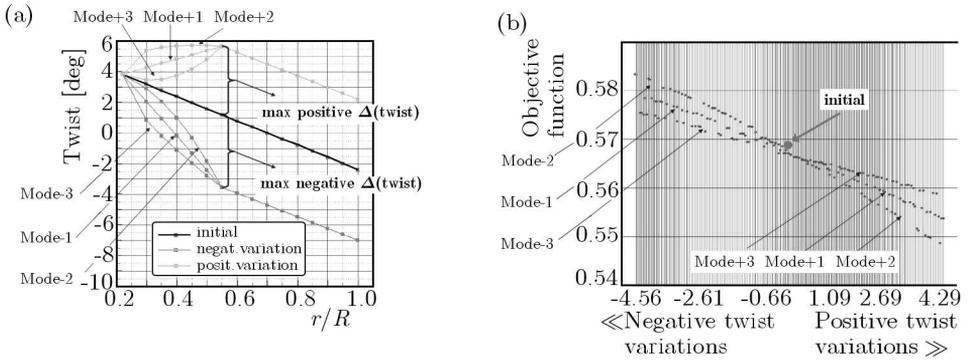

Fig. 17. (a) Twist distributions: positive (light grey) and negative (grey), linear (mode 1) and parabolic (modes 2 and 3), (b) objective function; SMA actuator located between 0.5 and $0.568 r/R$

ator position. The results are sketched in Figs. 15b, 16b and 17b, respectively. By looking at the individual DOE results, the following conclusions can be drawn:

- negative twist variations result in performance improvements;
- the twist law affects significantly performance calculations;
- the twist law labeled as mode 2 offers the most significant performance gain;
- the maximum twist variation is necessary to get the maximum performance gain.

Finally, a summary of the most promising results is reported in Table 5 and the associated figures of merit are compared in Fig. 18. It clearly appears that

the actuator integrated in the range $r/R \in [0.9, 0.968]$, assures a better hover performance.

Table 5. Summary of the results

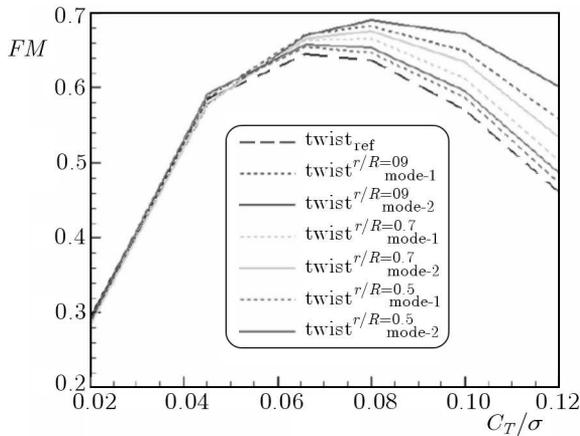| ID	Spanwise range where twist variations are possible	Maximum allowed twist variation	Objective function (max value)
Twist$_{\text{initial}}$	−	−	0.569
Twist$_{(\text{mode } 1)}$	$r/R = [0.22, 0.568]$	$-4.61°$	0.578
Twist$_{(\text{mode } 1)}$	$r/R = [0.22, 0.768]$	$-5.06°$	0.591
Twist$_{(\text{mode } 1)}$	$r/R = [0.22, 0.968]$	$-5.75°$	0.608
Twist$_{(\text{mode } 2)}$	$r/R = [0.22, 0.568]$	$-4.61°$	0.583
Twist$_{(\text{mode } 2)}$	$r/R = [0.22, 0.768]$	$-5.06°$	0.599
Twist$_{(\text{mode } 2)}$	$r/R = [0.22, 0.968]$	$-5.75°$	0.616

Fig. 18. Figure of merit comparison for the several SMA twist distributions

6. Prototype realisation and testing

In order to validate the numerical predictions, a SMA twist prototype has been designed and manufactured. As shown in the scheme in Fig. 29, it is constituted by:

- a SMA rod element; this component is clamped on three points along its extension; milling operations are required in the three interface zones with the clamps to transmit the best torque couple;

- SMA clamps; their aim is to transmit the SMA induced rotation to the two elastic lateral beams; they are directly in contact with the SMA element and constrain the beams, pressing them through electrical insulation layers disposed at the interface;

- elastic beams; they provide the restoring couple (whose torque rigidity is equivalent to the hypothetic blade instrumented with the twist device), acting when the SMA rod is cooled;

- beams connection representing a constraint to any radial displacement of the elastic beams

- layer electrical insulation;

- they, suitably pressed by the clamps, guarantee electrical insulation between the clamps and elastic beams and rotation transmission.

- insulation pivots; these elements hinder any radial translations of the beams and guarantee electrical insulation.
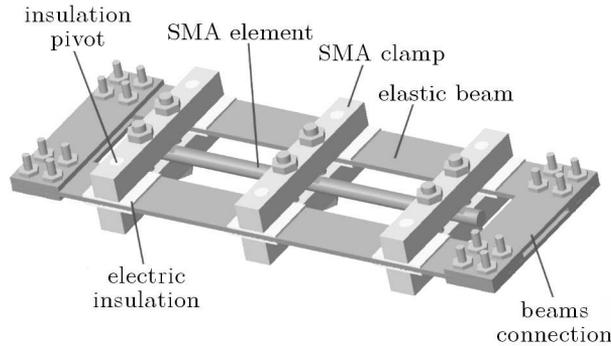

Fig. 19. Torque demonstrator sketch

According with the scheme and with reference to the specifications reported in Table 6, a real prototype has been manufactured. During the manufacturing process, a preliminary training phase has been necessary to keep constant SMA properties during operative life: the SMA rod has been mounted within a hydraulic machine (INSTRON) and subjected to load and unload cycles, up to reach the satisfying repeatability level. Then, the SMA edges have been connected to a home made machine and a 225 deg angular pre-deformation has been impressed; this latter value guarantees austenite into martensite transformation.

After fixing the rod in this deformed state, both to make easier the connection between SMA element and surrounding elastic plates and to maximize

Table 6. Main features of the prototypes

Plate spring dimensions	$0.16\,\text{m} \times 0.025\,\text{m} \times 0.002\,\text{m}$
Plate spring material	7075 T6 Aluminium alloy
SMA rod dimensions	Radius: 0.0025 m, length: 0.25 m
	(the effective no clamped length is of 0.16 m)
SMA rod material	NiTiNol (Ni: 55.5%, Ti: 44.5%)
Prestrained angle	100 deg

the transmittable torque couple through SMA dedicated clamps (see Fig. 19), three carvings have been made by grinding. This operation has been performed controlling local temperature by means of a cooling refrigerant gas, avoiding this way, thermal induced variations of the material properties.

Finally, after mounting the elastic plates around the SMA rod, one edge has been released, allowing for a partial rotation recovery (8.18 deg with respect to the clamped condition), resulting in a compromise between the structure and SMA elastic reactions. Residual stress will assure SMA return into the initial no-activated configuration, after cooling.
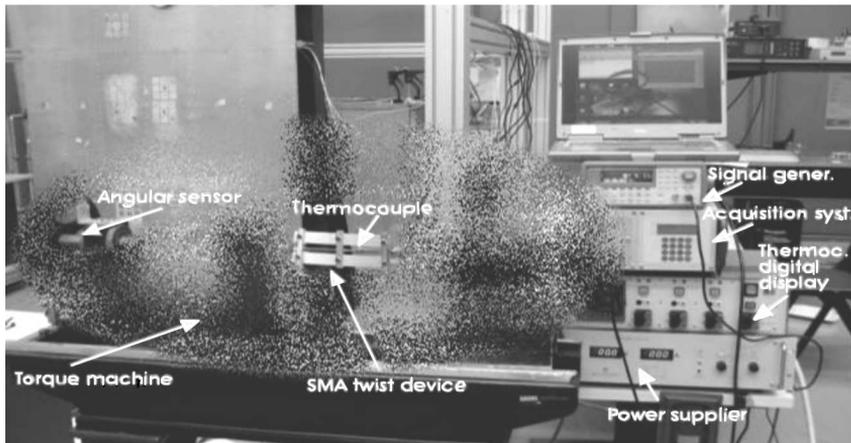

Fig. 20. Experimental setup

Once addressed manufacturing and preliminary training operations, a dedicated experimental setup (shown in Fig. 20) has been assembled, integrating the SMA device and mechanism in charge of twisting with:

- an angular sensor (electro-transducer) to measure all the rotations occurring in pre-test (preparation of the SMA rod, by inducing an initial strain) and test phases;

- a thermocouple (K typology) bonded on the rod to measure the actual temperature;

- an acquisition system (imc CRONOS-PL) to collect data provided by the angular sensor and the thermocouple;

- a power supplier (Delta Elektronika, SM 45-70D) to heat the SMA rod by Joule effect;

- a signal generator (Agilent 33220A) to generate a logical signal (a square wave) to command the switch on (heating phase) and switch off (cooling phase) of the SMA element, for cyclic tests;

- a thermocouple digital displayer, to have a digital estimate of the actual temperature.

The purpose of such an apparatus has been the estimate of the SMA element ability of transmitting rotations to the surrounding elastic structure vs. activation cycles. A logical signal has been used to command the supplier within a 1500 s period cycle: in practice a power of 91 W (70.0 A×1.3 V) has been supplied only in the early 300 s of any cycle to achieve maximum temperature of 200°C (above which no further rotations have been observed), and then the SMA element has been let cool by natural convection, up to reach the initial room temperature (27.0°C). In Fig. 21, on the left, both temperature and an-
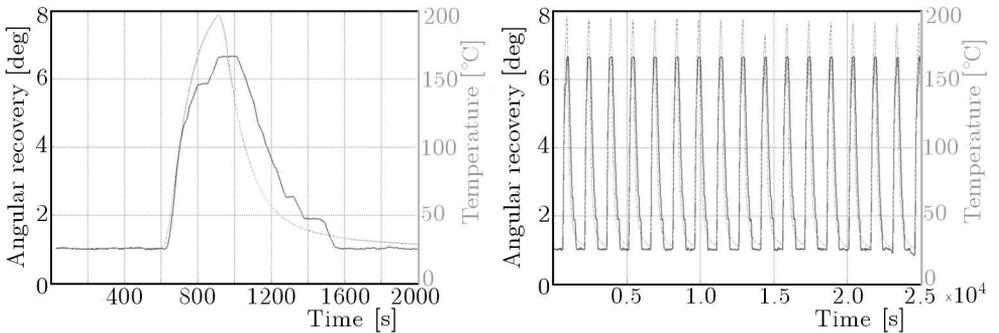

Fig. 21. Single working cycle: angular rotation and temperature vs. time

gular rotations within a single cycle are plotted vs. time. In the same figure, on the right, the device behaviour vs. 16 cycles have been reported, demonstrating that no appreciable performance variations in terms of transmitted couple occurred. A 6 deg maximum angular rotation has been achieved for a temperature of 198°CC. To deduce the transmitted moment, a dedicated FE model of the surrounding elastic structure has been realised (see Fig. 22); the required moment is equal to the torque couple producing the same rotation

(6 deg) experimentally measured. This value resulted in 21.6 Nm, corresponding to the maximum of stress 214 MPa within the spring. Finally, in Fig. 23, the on and off states of the SMA device have been compared.
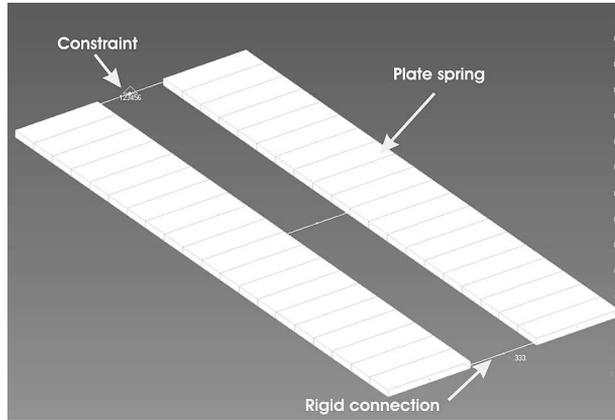

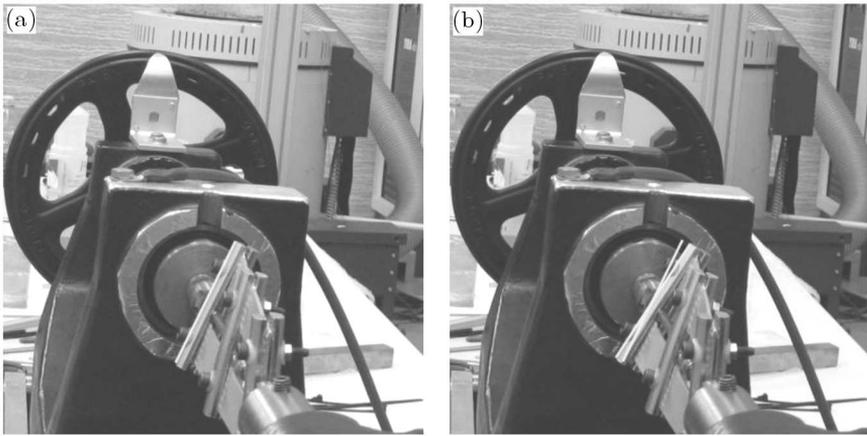Fig. 22. FE model of laboratory demonstrator surrounding structure

Fig. 23. SMA device: before actuation (a), after actuation (b)

7.   Conclusions and further steps

The activities described in this work have been developed within FRIEND-COPTER European Frame, aimed at mitigating helicopter environmental impact. Among different strategies taken into account, the adaptive morphing of crucial blade geometric parameters, like the twist angle distribution and

the airfoil camber, has been considered. Due to the multidisciplinary nature of these topics (aerodynamics, aeroelasticity, structures, over-all flight performance), dedicated design strategies, involving several software typologies, have been identified and implemented. Thus, an optimisation process has been addressed to finding out optimal camber modifications, fitting, in terms of lift, the drag and pitching moment coefficients, different flight regimes occurring during helicopter mission. The adopted numerical simulation flowchart is constituted by a meshing code that does not regenerate computational grids but smoothly deforms the high quality reference grid using arc length transfinite interpolation; then CFD computations are performed by modelling turbulence transport quantities through a $k - \omega$ model. The achieved results, driven by the necessity of reducing the action of needed actuator, remain within a small displacement field.

After facing the morphing of the airfoil, representing a 2D part of the blade, the author's attention has focused on the control of a 3D geometric parameter: the twist angle. The inspiring idea is to induce a suitable steady torque onto the blade during specific flight conditions (e.g. hover), thus improving performance. The high integration level guaranteed by SMA large transmittable forces-deformations per unit volume, has led to consider a monolithic structure, a rod element aimed at transmitting torque. The heating of this SMA element integrated along the span-wise direction, suitably angularly pre-deformed during manufacturing, leads to strain recovery (coherent with the Shape Memory property), that is transmitted to the blade surrounding structure. At first, a predictive investigation has been addressed to find the optimal twist distribution ensuring better performance at different disk load conditions. Basing on the acquired information in terms of needed twist angle amplitude, the actuator design task has been dealt with. Transmittable twist performance has been predicted through a dedicated FE numerical tool, implementing the Brinson SMA model. To validate the numerical approach, an experimental prototype has been built and characterised through a dedicated setup, guaranteeing the monitoring of fundamental state parameters like temperature, angular rotation, time, power supply and transmitted couple. Finally, the performance achievable at several integration levels of the SMA rod along the span has been predicted by demonstrating that an adaptive twist may assure the extension of optimal values of the figure of merit. Further activities will be performed on the mentioned morphing topics. Actual numerical specimens and conceptual laboratory demonstrators will be complemented by tailored prototypes reproducing both the adaptive camber airfoil and the blade static twist. Problems like the integration of actuators (deriving

e.g. from the specific nature of SMA materials) will be considered during executive design phase. Finally, an experimental campaign aimed at appreciating actuators ability of producing required morphing in presence of inertial and aerodynamic loads and highlighting predicted performance improvement will be carried out.

References

1. ALTMIKUS A.A., BAILLY B.J., 2005, *FRIENDCOPTER Report on Reference Rotor*, Deliverable No.: D 5.1-2, 17 May

2. BRINSON L.C., BEKKER A., HUANG M., 1996, Deformation of shape memory alloys due to thermo-induced transformation, *J. of Intelligent Material Systems and Structures*, **7**, 1, 97-107

3. BUEHLER W.J., GILFRICH J.V., WILEY R.C., 1963, Effect of low-temperature phase changes on the mechanical properties of alloys near composition TiNi, *Journal of Applied Physics*, **34**, 1475

4. CHOPRA I., 2002a, Review of state of art of smart structures and integrated systems, *42nd AIAA/ ASME/ASCE/AHS/ASC Structures, Structural Dynamics, and Materials Conference*, Seattle, WA, *AIAA Journal*, **40**, 11

5. CHOPRA I., 2002b, Status of application of smart structures technology to rotorcraft systems, presented at the innovation in rotorcraft technology, *Royal Aeronautical Society, London, UK, June 25-26, 1997* and *AHS Journal*

6. DAVIDSON F.M., LIANG C., LOBITZ D.W., 1996, Investigation of torsional shape memory alloy actuators, *Proc. SPIE*, **2717**, 672-682, *Smart Structures and Materials 1996: Smart Structures and Integrated Systems*, Inderjit Chopra (Edit.)

7. DRIKAKIS D., 2003, Advances in turbulent flow computations using high-resolution methods, *Progress in Aerospace Science*, **39**, 405-424

8. Drikakis D., Durst F., 1994, Investigation of flux formulae in shock wave turbulent boundary layer interaction, *International Journal for Numerical Methods in Fluids*, **18**, 385-413

9. Drikakis D., Tsangaris S., 1993, On the solution of the compressible Navier-Stokes equations using improved flux vector splitting methods, *Applied Mathematical Modelling*, **17**, 282-297

10. Enenkl B., 1988, *1/2.5 Scaled Model Rotor of the Hingeless BO105 Main Rotor*, MBB Technical Documentation, 26.10.1988

11. Jaeggi D.M., Asselin-Miller C.S., Parks G.T., Kipouros T., Bell T., Clarkson P.J., 2004, Multi-objective parallel tabu search, *Lecture Notes in Computer Science*, **3242**, 732-741

12. Jayasimha A., Chopra I., 2003, Behavior of torsional shape memory alloy actuators, *44th AIAA/ASME/ASCE/AHS Conference*, Norfolk, Virginia

13. Liang C., Davidson F.M., Schetky L.M., Straub F.K., 1996, Applications of torsional shape memory alloy actuators for active rotor blade control: opportunities and limitations, *Proc. SPIE*, **2717**, 672-682, *Smart Structures and Materials 1996: Smart Structures and Integrated Systems*, Inderjit Chopra (Edit.)

14. Liang C., Rogers C.A., 1990, One-dimensional thermomechanical constitutive relations for shape memory material, *J. of Intelligent Material Systems and Structures*, **1**, 2, 207-234

15. *OPTIMUS, Optimization environment*, Software Package, Ver. 5.2, Noesis solutions, Belgium, 2006

16. Pagano A., 2003, *Investigations within the ADYN Project: a Year of Activities*, CIRA doc. N. CIRA-TR-02-503, January

17. Prahlad H., Chopra I., 2002, Chracterization of SMA Torsional Actuators for Active Twist of Tilt Rotor Blades, *43rd AIAA/ASME/ASCE/AHS/ASC Conference*, Denver, Colorado

18. Prahlad H., Chopra I., 2007, Modeling and experimental characterization of SMA torsional actuators, *Journal of Intelligent Material Systems and Structures*, **18**, 1, 29-38

19. Shu C.W., 1997, *Essentially Non-Oscillatory and Weighted Essentially Non-Oscillatory Schemes for Hyperbolic Conservation Laws*, NASA CR-97-206253

20. Schultz K.J., Splettstoesser W., Junker B., Wagner W., Schoell E., Arnauld G., Mercker E., Pengel K., Fertis D., 1996, *A Parametric Wind Tunnel Test on Rotorcraft Aerodynamics and Aeroacoustics (HELISHAPE) – Test Documentation and Representative Results*, DLR IB 129-96/25, June

21. STEGER J.L., WARMING R.F., 1981, Flux vector splitting of the inviscid gas-dynamic equations with application to finite-difference methods, *Journal of Computational Physics*, **40**, 263-293

22. TANAKA K., 1986, A Thermomechanical sketch of shape memory effect: one-dimensional tensile behaviour, *Res. Mech.*, **18**, 3, 251-263

23. TORO E.F., SPRUCE M., SPEARES W., 1994, Restoration of the contact surface in the HLL-Riemann solver, *Shock Waves*, **4**, 1, 25-34

24. WARMBRODT W., PETERSON R.L., 1984, Hover test of a full-scale hingeless rotor, *NASA Technical Memorandum*, **85990**

25. www.friendcopter.org, Integrated Project of the European 6th Framework Programme: *Integration of Technologies in Support of a Passenger and Environmentally Friendly Helicopter*

26. www.pointwise.com/gridgen

Strategie aktywnego kształtowania profilu łopat helikoptera w celu redukcji negatywnego wpływu ich pracy na środowisko

Streszczenie

Wymóg jak najmniejszej uciążliwości helikopterów na otaczające środowisko został wyartykułowany w projekcje europejskim FRIENDCOPTER, w którym kilka zagadnień (takich jak redukcja hałasu, drgań, obniżanie zużycia paliwa) poddano równoległym badaniom, łącznie z problemem odpowiedniego kształtowania profilu łopat wirnika głównego do osiągnięcia tych celów. W prezentowanej pracy uwagę skupiono na ograniczaniu środowiskowej uciążliwości helikopterów poprzez przyjęcie dwóch koncepcji kształtowania łopat wirnika – aerodynamiczną optymalizację przekroju łopaty, której kształt może być deformowany za pomocą aktuatorów oraz wprowadzenie stopów z pamięcią kształtu (SMA) do skręcania profilu łopaty, co pozwala na rozszerzenie obwiednich osiągów helikoptera. Drugie rozwiązanie zostało oparte na zastosowaniu prętów SMA zintegrowanych z łopatą w kilku miejscach wzdłuż jej długości. Aktuatory SMA generują pary momentów skręcających przy podgrzaniu. Modelowanie tego efektu opisano za pomocą metody elementów skończonych (przy użyciu modelu Brinson SMA i oprogramowania MSC/Marc). Na koniec przedyskutowano wydajność wirnika głównego dla helikoptera w zawisie przy włączonym i wyłączonym układzie sterowania. Podkreślono korzyści uzyskane z wzdłużnego wkomponowania w łopatę wirnika kilku aktuatorów SMA.